International Journal of Precision Engineering and Manufacturing-Green Technology
https://doi.org/10.1007/s40684-022-00421-3

Online ISSN 2198-0810
Print ISSN 2288-6206

REGULAR PAPER

Laser Patterning Technology Based on Nanosecond Pulsed Laser for Manufacturing Bifacial Perovskite Solar Modules

Bo-Qian Lin[1] · Chao-Peng Huang[1] · Kuo-Yo Tian[2] · Pei-Huan Lee[2] · Wei-Fang Su[2] · Li Xu[1]

Received: 21 August 2021 / Revised: 3 November 2021 / Accepted: 4 January 2022

Abstract
Bifacial semi-transparent perovskite (PVSK) solar cell is a promising candidate to achieve high photo-electrical conversion efficiency (PCE) in a tandem structure with Si solar cells. The gap between lab-scale cells and large area modules needs to be closed using innovative patterning technology. In this paper we demonstrate that a single nanosecond pulsed laser (wavelength 532 nm, pulse duration 7 ns) can be used to perform all scribing processes, i.e. P1, P2 and P3, to manufacture PVSK solar modules. Compared to picosecond or femtosecond lasers reported in the literature, our approach has the advantages of high stability and low cost, and is thus applicable to large scale manufacturing of PVSK solar modules. Detailed laser processing parameters such as laser power and overlap ratio etc. have been studied to achieve optimal results for each scribing process. A mini module with two cells was fabricated on a 2×2 cm^2 substrate, showing an active area efficiency of 12.5%, FF of 72.4%, and high GFF of 94%.

Keywords Laser patterning · Laser scribing · Perovskite solar module · Bifacial perovskite solar cell

1 Introduction

Recently perovskite (PVSK) solar cells gain extensive attentions in the photovoltaic (PV) field owing to its exceptional intrinsic optoelectronic properties, such as high absorption coefficient, long exciton lifetime and diffusion length. The first PVSK solar cell was demonstrated in 2009 by Miyasaka et al., with a power conversion efficiency (PCE) of 3.81% [1]. Since then the PCE has increased dramatically [2–6]. In 2020, a single junction PVSK solar cell with PCE of 25.5% was recorded by NREL, rivaling the thin film solar cell (CIGS: 23.4% and CdTe: 22.1%) and approaching the single-crystal silicon solar cell (26.1%). Moreover, the durability has been increased from a few minutes to the order of 10,000 h [7], promoting the possibility of commercialization. Meanwhile, to get larger and more uniform films, blade-coating [8–11], slot-die [12–15], spray coating [16, 17], and other deposition methods were developed [18, 19].

Despite the extensive studies and advances one huge gap must be closed before the transition from lab-scale cells to commercialized modules can be realized. With the increasing area of solar cells, the internal electrical resistance increases substantially resulting in significant loss of output power. A module structure with many small area cells connected in series is introduced to reduce the internal resistance, i.e. monolithic integration method. Three scribing lines named P1, P2 and P3 are required to connect all cells in series as shown in Fig. 1. P1 insulates the front electrode of each cell, and P2 allows the top electrode to contact with the front electrode, and P3 isolates the back electrode. The region between P1 and P3 is called “dead zone” or “dead area” as the area is not active and do not contribute to power conversion. Geometry fill factor (GFF) is defined as the ratio of active area to the total module area. The larger the dead area is, the lower the GFF and module efficiency are. Therefore, one of the important goals in module fabrication is to minimize the dead area and improve GFF.

To date, a few patterning approaches have been demonstrated. For instance, Matteocci et al. used chemical etching to form P2 and pasted a mask during evaporating the back electrode to get P3 [20]. Yang et al. cut P2 and P3 with

✉ Wei-Fang Su
suwf@ntu.edu.tw

✉ Li Xu
lixus@ntu.edu.tw

[1] Department of Mechanical Engineering, National Taiwan University, Taipei, Taiwan

[2] Department of Material Science and Engineering, National Taiwan University, Taipei, Taiwan

Published online: 31 January 2022

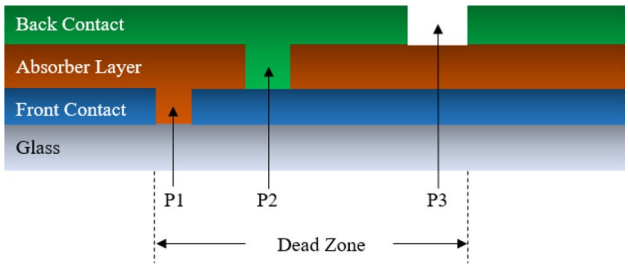

Fig. 1 Schematic diagram of three scribing lines P1, P2 and P3 for monolithic integration of solar modules

mechanical scribing [21]. Hiroshi and Takayuki scribed P2 with mechanical scribing followed with laser treatment to reduce the series resistance and to improve the contact [22]. However, the methods of mechanical scribing or chemical etching have limited capability to precisely control the line width as well as the line spacing, resulting in an undesired increase of the dead area. In addition, mechanical scribing of P2 cannot completely remove all the material above the bottom electrode. Residual material could lead to a substantial increase of series resistance in the module [23].

Recently, many research efforts applied laser on module fabrication because of its high precision and selectivity [24–27]. As a non-contact process and wavelength selective method, laser ablation on perovskite layer has been investigated [28–30]. The first full-laser patterned PVSK module was reported by Moon et al., with a PCE of 6.6% on an aperture area of 5 cm^2 with an aperture ratio of 84% [31]. Palma et al. demonstrated a 95% aperture ratio module with a pico-second laser [32]. With ultra-fast pulse laser, the pulse duration is shorter than the electron cooling time, typically in a few pico-seconds, which means electrons do not have enough time to transfer the energy to the lattice of solid, and a direct solid to vapor transition takes place [33]. If the laser pulse is in the order of femtosecond, a cold interaction with the matter process occurs, without other correlated negative effects, such as heat accumulation [34]. As a trend, more and more scholars use ultrashort pulse lasers in the fabrication of perovskite modules [32, 35, 36]. However, ultrafast lasers are expensive which would significantly increase the fabrication cost.

In this study we developed laser patterning technology based on a nanosecond pulsed laser with a wavelength of 532 nm and successfully demonstrated fabrication of semi-transparent bifacial perovskite solar modules, with the highest PCE of 12.5% on an aperture area of 1.1 cm^2 and a high GFF of 94%.

2 Experiment

2.1 Materials Preparation

NiO_x was used as hole transport layer (HTL). The NiO_x precursor solution was prepared in ambient air. 124.4 mg Nickel acetate tetrahydrate (Ni $(CH_3COO)_2{\cdot}4H_2O$, 99.0%, Showa Chemical) was dissolved in 1 mL of ethanol (99.99%, Fisher Chemical). The solution was stirred at 70 ℃ for 20 min and then adding 30 µL ethanolamine (99%, Acros Organic). Before the coating process, the green solution was filtered with 0.22 µm PTFE syringe filters.

Perovskite precursor, electron transfer layer (ETL) and work function modifier layer (WFL) were prepared 12 h before coating process in nitrogen environment. The $MAPbI_3$ precursor which used as absorber layer was prepared by dissolving 176.6 mg methylammonium iodide (MAI, STAREK Scientific Co., Ltd) and 506 mg lead iodide (PbI_2, 99%, Acros Organic) in the 840 µL of solvent mixture of dimethyl sulfoxide (DMSO, 99.9+%, Acros Organic) and *N*,*N*-dimethylformamide (DMF, 99.8%, Acros Organic) with the volume ratio of 2:5. For ETL, the [6, 6]-pheyl-C61-butyric acid methyl ester ($PC_{61}BM$, 99.5%, Solenne B.V.) was used. 20 mg $PC_{61}BM$ was dissolved in 1 mL chlorobenzene (CB, 99+%, Acros Organic) and was filtered with 0.22 µm PTFE syringe filters before using. The concentration of 0.1 wt% of polyethyleneimine (PEI, branched, Average M_n 10 k, Sigma Aldrich) was used as WFL. 100 mg PEI was dissolved in 1.46 mL of isopropanol (IPA, 99.5%, Acros Organic) to get 8 wt% PEI solution. Then, 10 µL of 8wt% solution was added to 790 µL of IPA to obtain 0.1 wt% PEI solution.

The TBAOH-SnO_2 nanoparticles was used as WFL and buffer layer [37]. First, SnO_2 nanoparticles were synthesized by the solvothermal method. Typically, adding 3.12 g of $SnCl_4$ (Sigma Aldrich) to 20 mL of the solvent mixture of benzyl alcohol (99.0%, Acros Organic) and toluene (99.8+%, Acros Organic) with the volume ratio of 3:1 as the precursor. Then, transferred the precursor solution to a Teflon-lined autoclave and heated in an oven at 180 ℃ for 12 h. After the reaction, a centrifuge was used to collecting the white precipitate. The white precipitate was then washed once with diethyl ether (99.0%, Fisher Chemical) and twice with ethanol (99.99%, Fisher Chemical). Second, in order to get OA-SnO_2 suspension, the synthesized SnO_2 nanoparticles were re-dispersed in 5 mL of chloroform (99.0+%, Acros Organic) and 1 mL of oleic acid (OA, 90%, Sigma Aldrich) to form milky suspension. During the ultrasonication, 1 mL of butylamine (BA, 99.5%, Sigma Aldrich) was added to obtain a transparent suspension. By adding acetone (99.0%, Alfa Aesar) to wash out excess OA and BA can purify the OA-SnO_2 suspension,

and then centrifuged and re-dispersed in chloroform with a concentration of 200 mg/m. Finally, after getting the pure OA-SnO_2 nanoparticles, a facile ligand exchange method was applied to replace the insulating OA molecule on the surface of SnO_2 nanoparticles with tetrabutylammonium hydroxide 30-hydrate (TBAOH, 95+%, Sigma Aldrich). Briefly, 50 µL of OA-SnO_2 suspension was added into 5 mL of the mixture of dichloromethane solution (99.8+%, Acros Organic) and boron trifluoride etherate (BF3-OEt_2, 98.0+%, Alfa Aesar). The precipitate was collected by centrifugation and added into 1 mL of TBAOH solution (30 mg/mL in ethanol). Then, adding hexane (99+%, Acros Organic) to obtain pure tetraalkylammonium hydroxide capped SnO2 nanoparticles and collecting precipitate by centrifugation. The nanoparticles were dispersed in 1 mL of TBAOH solution (7.5 mg/mL in ethanol) again, and repeat the precipitate process. Finally, the collected TBAOH-SnO_2 nanoparticles were dispersed in 1 mL of TBAOH solution (1.875 mg/mL in ethanol).

2.2 Solar Cell Fabrication

First, we cleaned glass substrates coated with fluorine-doped tin oxide (FTO, sheet resistance: 7 Ω/sq). The FTO glass was sequentially immersed in soapy water, ammonia hydrogen peroxide solution (water:hydrogen peroxide:ammonia = 5:1:1 in volume), methanol, and isopropanol, cleaned ultrasonically, followed by a 15 min UV–ozone treatment. The NiO_x sol–gel solution was was spin-coated at 4000 rpm, 20 s as HTL [38]. After the NiO_x layer was annealed at 340 °C for 40 min, the perovskite precursor was then spin-coated on it at 4500 rpm for 30 s in a glove box filled with nitrogen. At 15th second of the spin-coating process 300 µL of diethyl ether (DEE, 99.0%, Fisher Chemical) was dropped onto the surface to wash out the extra solvent and formed a transparent intermediate perovskite phase. Then sample was annealed on a hot-plate at 65 °C for 1 min and then 105 °C for 2 min to form α-phase perovskite film. The $PC_{61}BM$ solution was spin-coated at 1000 rpm 30 s as ETL. Afterward, as prepared SnO_2-TBAOH [37] suspension was spin-coated onto $PC_{61}BM$ layer at 1500 rpm 30 s as WFL and buffer layer. Then, PEI in isopropanol was spin-coated at 3000 rpm 20 s onto SnO_2 -TBAOH layer. Finally, back electrode of indium cerium oxide (CeO_2:In_2O_3, ICO) with thickness of 300 nm was deposited by a sputter (Kao Duen Tec. Co.). The size of the lab-scale solar cell was 0.09 cm^2.

The structure of device is shown in Fig. 2.

2.3 Module Fabrication

A Nd:YAG laser with a wavelength of 532 nm and a pulse duration of 7 ns with a fixed frequency of 7500 Hz was used to fabricate P1 P2 and P3. A 2× objective lens was used to focus the laser beam. Laser beam size at the focal point was measured to be 126 µm at the full width half maximum (FWHM). All laser processes were operated at the focal point.

For module fabrication, laser scribing of front electrode FTO (P1) was applied immediately after cleaning of FTO glass. Following the same steps as shown in part B, the absorber layer as well as HTL and ETL were fabricated. Then laser scribing of the absorber layer, HTL and ETL (P2)

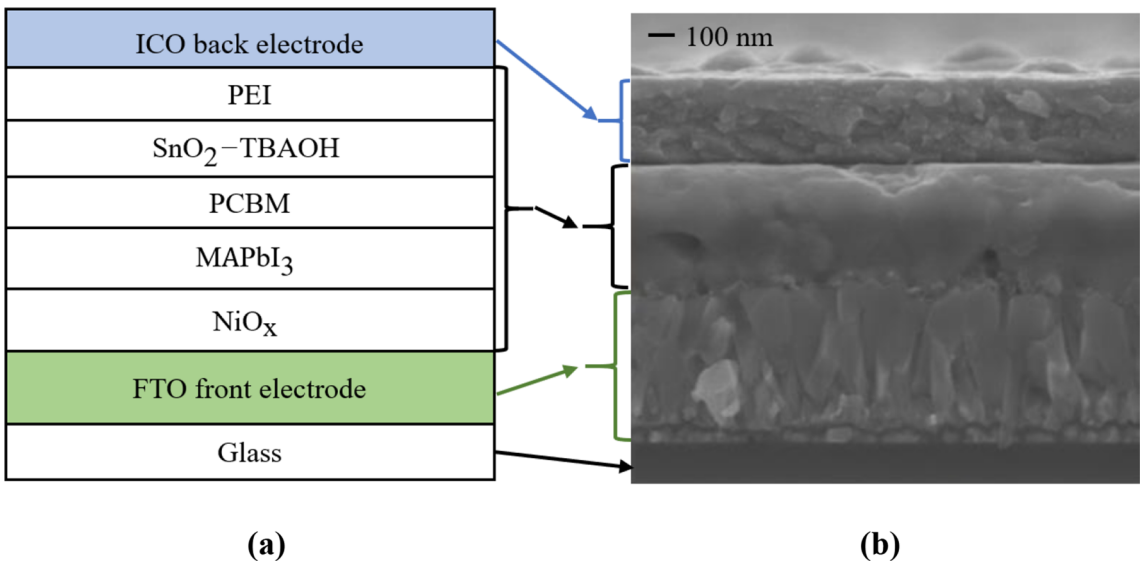

Fig. 2 **a** Schematic diagram of device structure of perovskite solar cell in this study; **b** SEM cross-section image of bifacial perovskite solar cell

was performed. After the back electrode ICO was deposited, the laser scribing (P3) was applied to isolate the ICO films.

2.4 Characterization

J–V curves of devices and modules were measured by a voltage source meter (Keithley 2410) under an AM 1.5 G solar simulator (Yamashita Denso YSS-50A-400A) with an irradiation of 1000 W/m^2. SEM images of surface morphology were obtained by scanning electron microscopy (SEM, JEOL JSM6510). Elemental analyses were performed by energy-dispersive X-ray spectroscopy (EDS, JEOL JSM6510). Transfer line method (TLM) was applied to characterize the contact resistance at P2 line.

3 Results and Discussion

Nanosecond pulse laser is essentially different in mechanisms of material ablation from pico-second or femto-second lasers. With ultra-fast pulse laser, the pulse duration is shorter than the electron cooling time, typically in a few pico-seconds, which means electrons do not have enough time to transfer the energy to the lattice of solid, and a direct solid to vapor transition takes place. In the order of nano-seconds electrons absorb laser energy and transfer it to the lattice. A typical solid–liquid–vapor process occurs and an area called heat affect zone is generated where laser power density is not high enough to ablate the material, but melt and heat the area. By adjusting laser processing parameters such as laser fluence, scan speed and overlap ratio one can control the heat affect zone to an acceptable range.

The wavelength of 532 nm is chosen because perovskite has high absorption coefficient to visible light, so that with green light laser can effectively heat up the perovskite layer and remove the material with minimum damage to the electrode in P2 processes. Although FTO and ICO films do not absorb the 532 nm light as strong as perovskite layer, they can still be removed when the light intensity is high enough.

3.1 Part I. Laser Scribing of P1 Line

Laser scribing of FTO film was to isolate top electrode of each cell. The parameter laser power density used in the discussion was defined as the fluence of each laser pulse divided by the product of pulse duration and the area of the laser beam.

High scan speed was used to form non-overlapped ablation spots on FTO film for the purpose of study. SEM images of the ablated spots with different power density 8.78×10^5 kW/cm^2 and 3.29×10^6 kW/cm^2 were shown in Fig. 3. The ablation mechanism involves the melting and evaporation of the material by the absorption of laser energy as evidenced by EDS analysis as shown in Table 1. The amount of tin residue at the center of the laser ablated spot was at 18.3 and 15.8 wt.% for laser power density of 8.78×10^5 kW/cm^2 and 3.29×10^6 kW/cm^2 respectively. The increase of the laser power density helped to reduce

Table 1 EDS elemental analysis of single pulse influence on FTO surface with 8.78×10^5 and 3.29×10^6 kW/cm^2 power density

Point location	Element (wt.%)		
	O	Si	Sn
Spectrum 1 in Fig. 2a	32.9	0	67.1
Spectrum 2 in Fig. 2a	55.0	26.6	18.3
Spectrum 1 in Fig. 2b	55.6	28.6	15.8

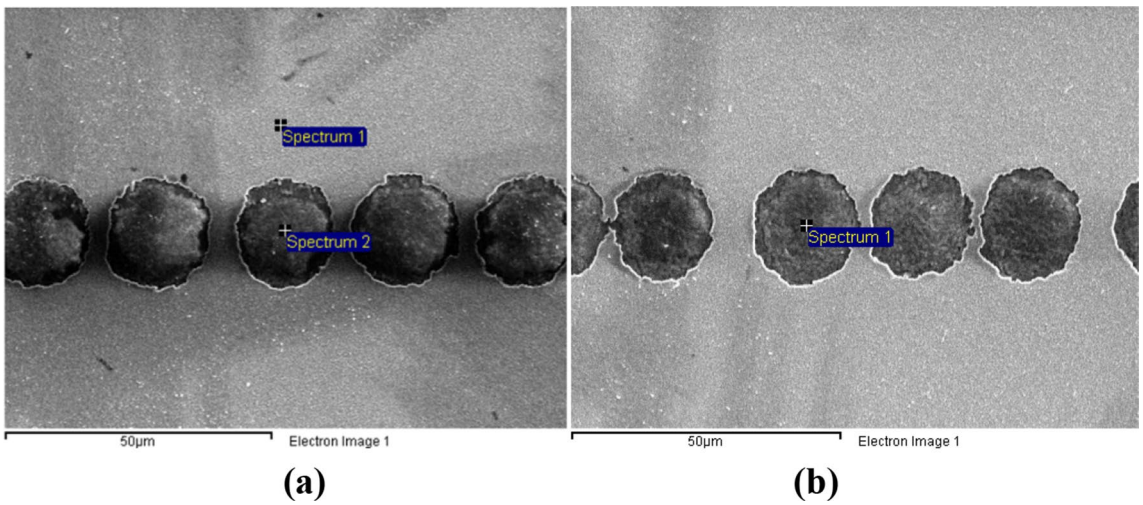

Fig. 3 SEM images of single pulse laser ablation of FTO films with laser power density of **a** 8.78×10^5 kW/cm^2 and **b** 3.29×10^6 kW/cm^2

the residue, the laser power density was not high enough to remove the FTO with one single laser pulse. Instead of going even higher laser power we found laser scanning with proper overlap ratio could help remove the FTO film completely. Overlap ratio was defined as the overlapped pulse region divided by the spot size (p/D) as shown in Fig. 4. It was determined experimentally by the laser pulse frequency and scan speed. SEM images of P1 scribing line at a constant power density 8.78×10^5 kW/cm^2 and different overlap ratio (a) 30% (b) 76% (c) 91% are shown in Fig. 5. Due to the incubation effect [39] FTO was completely ablated at 91% overlap ratio. EDS analysis results in Table 2 indicated there was no tin signal at center of scribed line. The resistance between the FTO films at two sides of P1 line was measured, showing FTO films were completely electrically isolated.

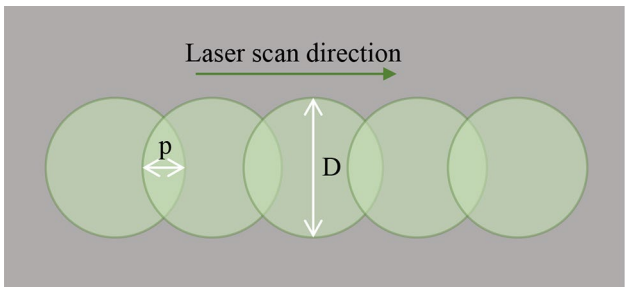

Fig. 4 Definition of overlap ratio, p divided by D

Table 2 Elemental analysis of P1 line scribed with (a) 30%, (b) 76%, (c) 91% overlap at fixed power density of 8.78×10^5 kW/cm^2

Overlap ratio	Element (wt.%)		
	O	Si	Sn
30%	58.7	29.1	12.2
76%	61.3	29.2	9.5
91%	70.4	29.6	0

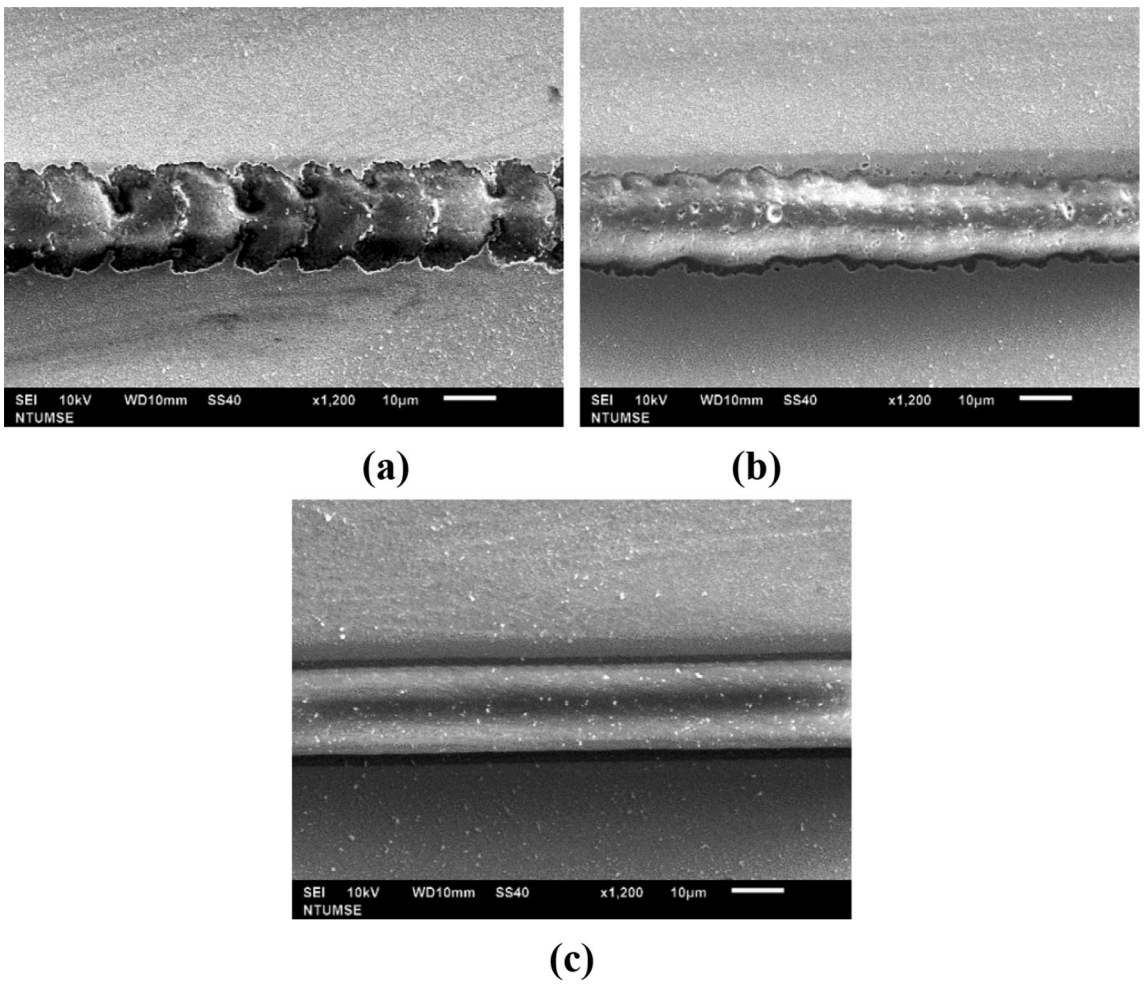

Fig. 5 SEM images of laser scribed P1 line with overlap ratio of **a** 30%, **b** 76%, **c** 91% and a fixed power density of 8.78×10^5 kW/cm^2

3.2 Part II. Laser Scribing of P2 Line

As the PVSK layer was very absorptive to the laser light at the wavelength of 532 nm, the laser power density for P2 scribing process was no surprisingly lower than that in P1 process. The SEM images of P2 scribing lines were shown in Fig. 6 at different power density from (a) 1.51×10^5, (b) 2.64×10^5, (c) 3.41×10^5, (d) 3.99×10^5 kW/cm^2 with overlap ratio fixed at 80%, and the corresponding EDS analysis results at the center of scribing lines are shown in Table 3. When the power density was 3.99×10^5 kW/cm^2 (case (d)), the Si signal which represents glass substrate was significant, implying that FTO was damaged and thinned. For the other three cases, the NiO_x (HTL) was removed as the weight % of Ni was about zero (within the measurement error), and the front electrode FTO was not damaged as the weight % of Sn were at 67% or more, similar to the EDS results of bare FTO film, and the weight % of Si was negligible. The data showed that there was a process window between $1.51 \sim 3.41 \times 10^5$ kW/cm^2 for laser power density with the overlap ratio of 80%.

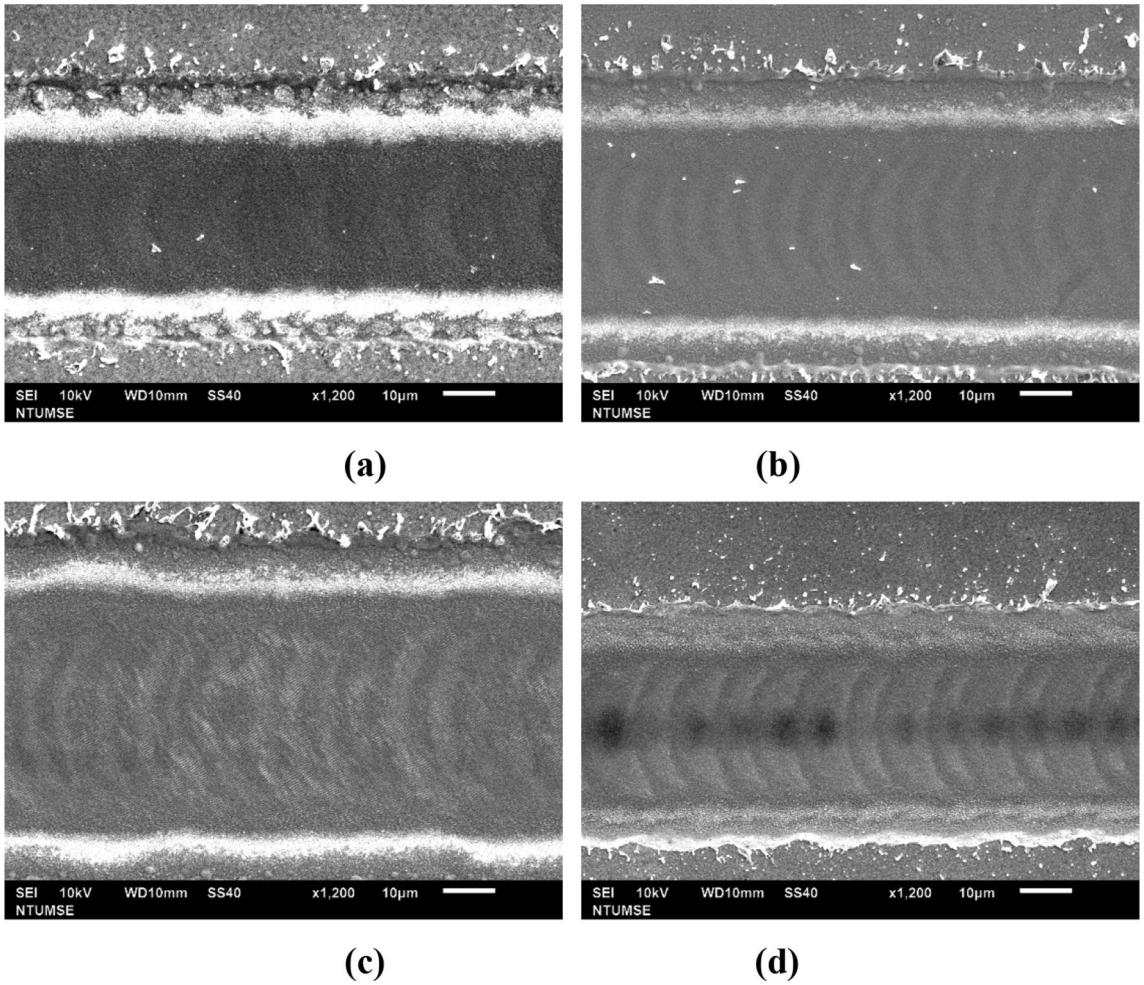

Fig. 6 SEM images of P2 line scribed with **a** 1.51×10^5, **b** 2.64×10^5, **c** 3.41×10^5, **d** 3.99×10^5 kW/cm^2 power density at 80% overlap ratio

Table 3 Elemental analysis of P2 line with different laser power density with fixed overlap ratio at 80%

Pulse fluence density (kW/cm^2)	Element (wt.%)					
	O	Ni	Sn	Si	Pb	I
(a) 1.51×10^5	33.1	0.2	67.4	0.3	0.1	–
(b) 2.64×10^5	32.0	1.6	68.5	0.3	–	0.6
(c) 3.41×10^5	28.5	–	70.2	0.5	–	–
(d) 3.99×10^5	40.7	–	37.0	19.7	–	0.1

When laser power density was fixed at 3.41×10^5 kW/cm^2, varying overp ratio affected the contact width of P2 lines. It should be noted that the contact width was not the same as line width since the heat affected zone was usually included when measuring line width in SEM or OM images, while the contact width only account for the area with clean removal of the materials which was determined by EDS results. A variation of overlap ratio was studied at the laser power density of 3.41×10^5 kW/cm^2 with results shown in Figs. 7 and 8. Figure 8f showed tin

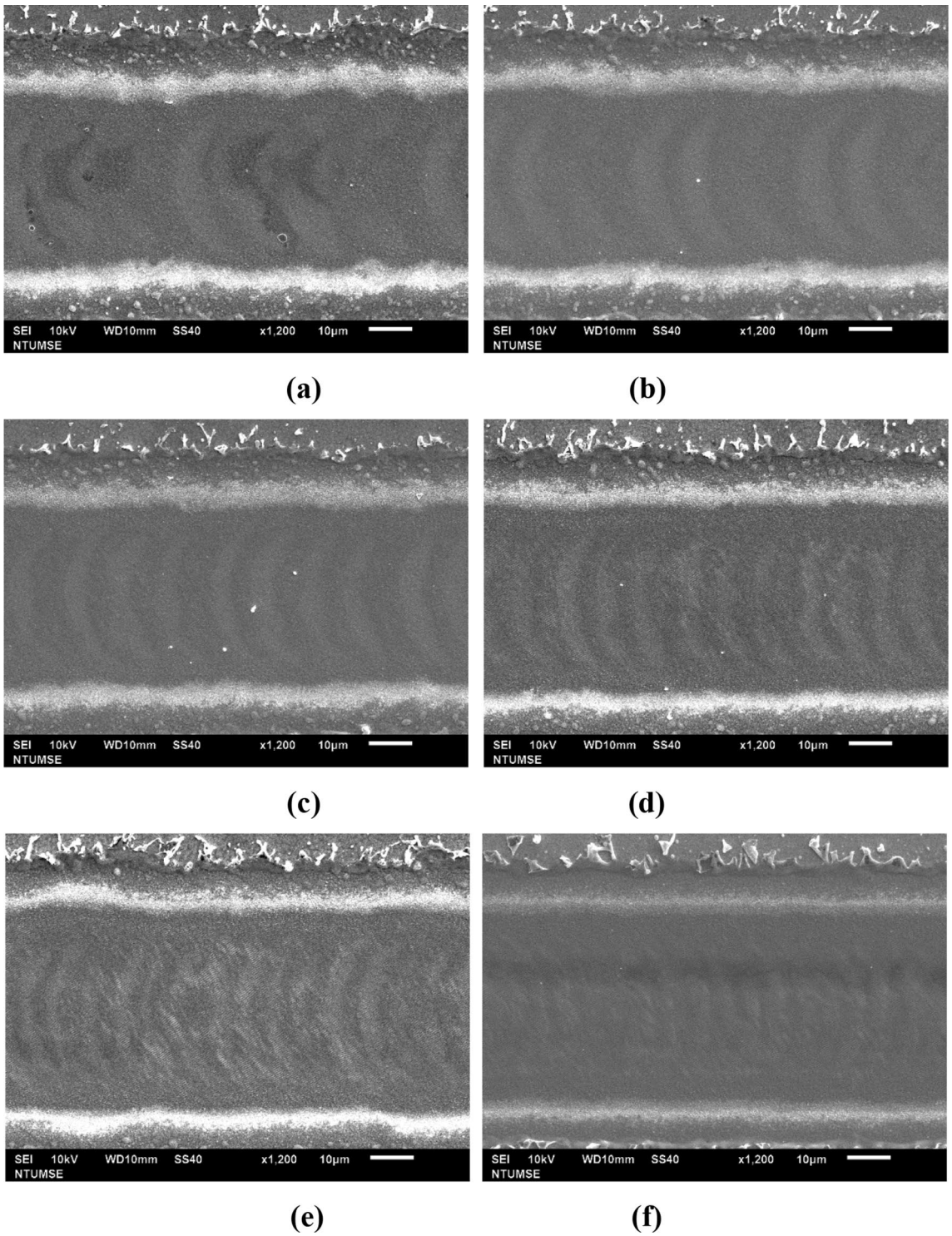

Fig. 7 SEM image of P2 line scribed with **a** 67, **b** 71, **c** 75, **d** 77, **e** 80, **f** 85% overlap ratio at fixed laser power density of 3.41×10^5 kW/cm^2

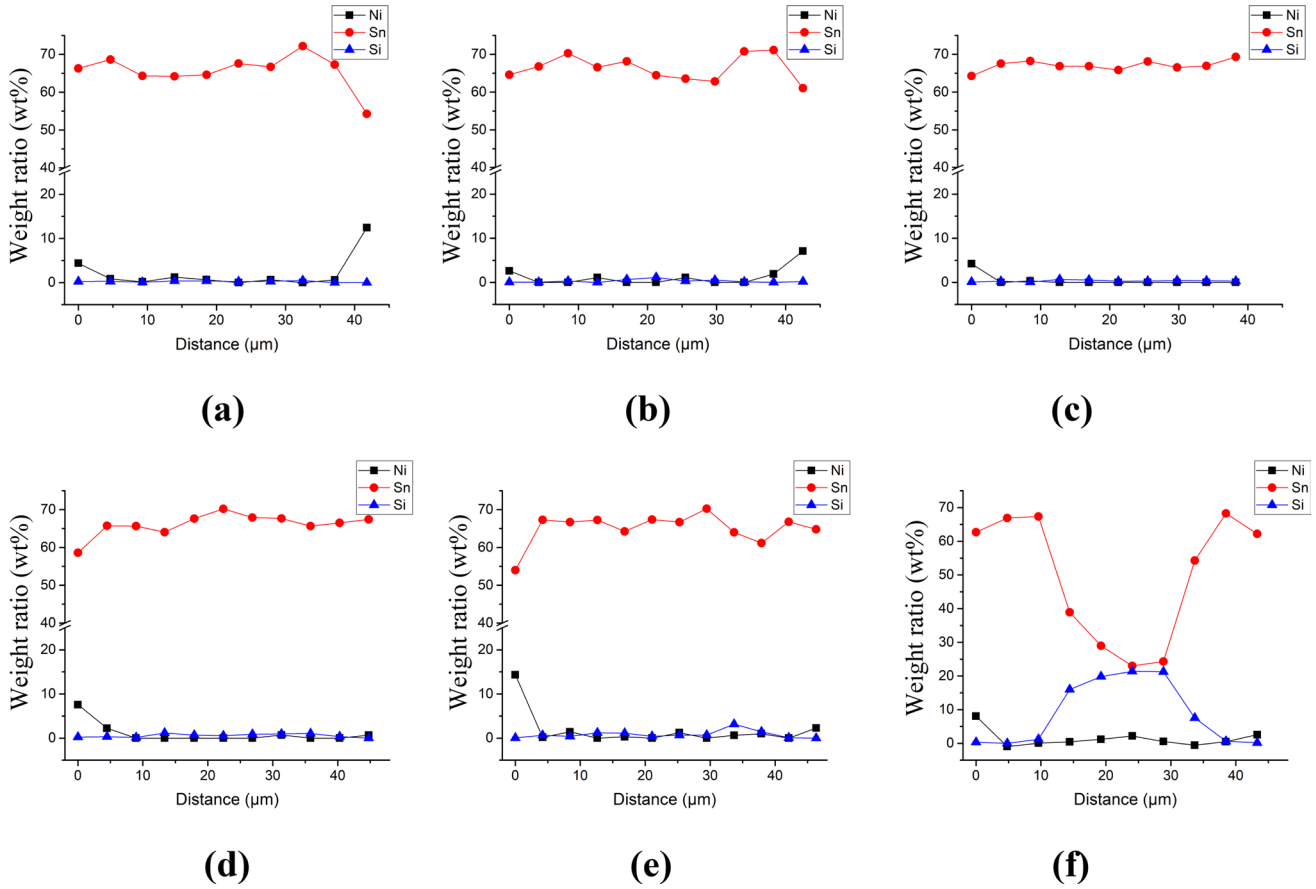

Fig. 8 Elemental analysis results of P2 line in cross section with different overlap: **a** 67, **b** 71, **c** 75, **d** 77, **e** 80, **f** 85% overlap ratio at fixed laser power density of 3.41×10^5 kW/cm^2

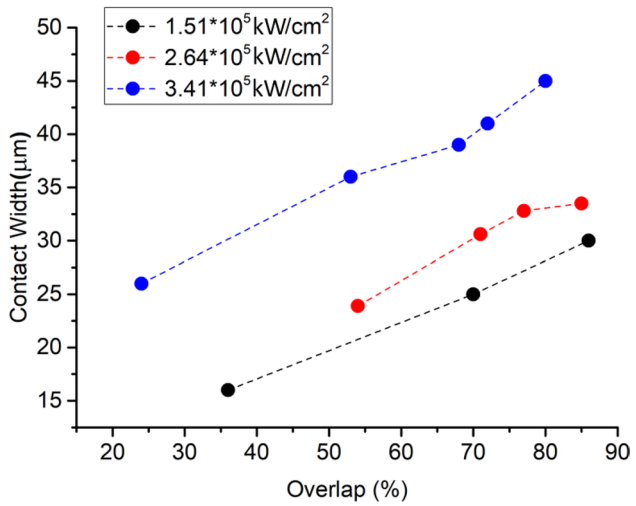

Fig. 9 Comparison of P2 contact width versus overlap ratio at different laser power density

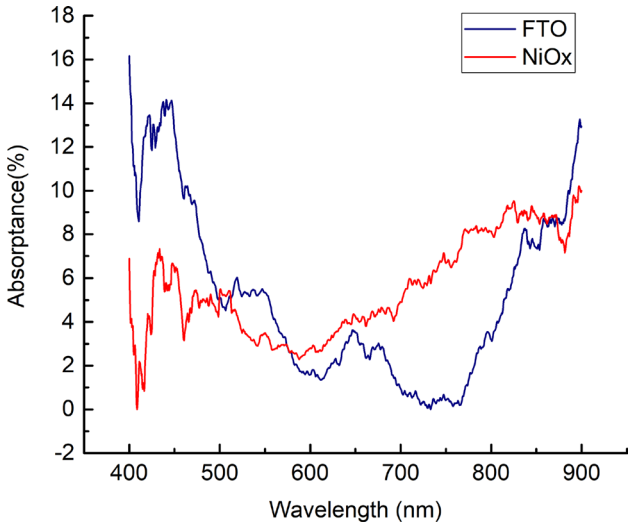

Fig. 10 Absorption of NiO_x and FTO layer in the wavelength of 400–900 nm

signal significantly dropped at the central of scribed line with an overlap ratio of 85% and the appropriate range of overlap ratio was between 67 and 80%. Taking the laser power density into consideration a correlation between overlap and contact width was summarized in Fig. 9. The contact width was increased with both laser power density and overlap ratio.

It was generally regarded that the process to remove NiO_x film from FTO film with laser irradiation was hard due to similar optical properties. As shown in Fig. 10 the absorptance of NiO_x layer and FTO in the visible wavelength range was similar and both very low at 532 nm wavelength (5.2 and 3.1% for FTO and NiO_x respectively), thus there is no selective optical absorption for the two materials. The mechanism of successful P2 scribing process by nanosecond-pulsed laser is actually because of the interface effect. FTO film was deposited on the glass substrate by physical vapor deposition (PVD) method, which results dense FTO films with good adhesion with the substrate. However, NiO_x was deposited on FTO film by spin coating at 70 °C and the adhesion to FTO was relatively weak. When the laser light was absorbed by the PVSK layer and the sudden increase of temperature resulted thermal–mechanical stress between the films, and the poor adhesion between NiO_x and FTO film resulted detachment of NiO_x from FTO film, while FTO film was intact due to stonger adhesion to the glass substrate. The difference in the adhesion strength of two interfaces allowed a process window to remove NiO_x without damaging FTO layer by nano-second laser scribing.

Transfer line method (TLM) was applied to measure contact resistance at P2 lines [25]. Specific contact resistance was determined by equation below:

$$R_c = \frac{\lambda_T \cdot R_{SH}}{W} \cdot \coth\left(\frac{W_{p2}}{\lambda_T}\right) = \frac{\sqrt{\rho_c \cdot R_{SH}}}{W} \cdot \coth\left(\frac{W_{p2}}{\lambda_T}\right)$$

With $\lambda_T = \sqrt{\frac{\rho_c}{R_{SH}}}$

R_{SH} is the sheet resistance of the bottom electrode,λ_T is the transfer length, W is length of contact area perpendicular to measuring direction and W_{p2} is the P2 line width or upper and lower electrode contact width. The specific contact resistance can be used to evaluate the results of different scribing processes.

Contact resistances by mechanical scribing with tweezers and laser scribing processes were compared as shown in Fig. 11 and Table 4. FTO directly contact with Ag was measured as the reference. For laser scribing process three contact widths 23, 30 and 41 µm were tested. It shows that the longer the contact width is, the lower the contact resistance is for laser scribing case. The specific contact resistance of 70 Ω·mm^2 was achieved with laser scribing process when the contact width was 30 µm or above. Tweezer scribed P2 line showed lower contact resistance owing to its much

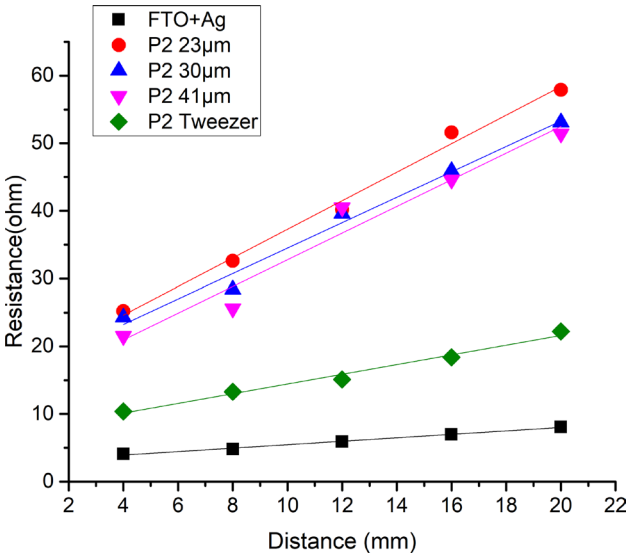

Fig. 11 TLM analysis of different contact condition. FTO + Ag, P2 line with 23/30/41 µm contact width respectively, and P2 line with tweezer

Table 4 TLM measurement results of different P2 recipe

	Transfer length (mm)	Contact resistance (Ω)	Specific contact resistance (Ω·mm^2)
FTO + Ag	1.72	1.46	20.81
P2 23 µm	4.85	8.09	140.3
P2 30 µm	3.16	7.87	70.29
P2 41 µm	3.07	6.54	66.35
P2 tweezer	4.75	3.64	158.84

wider P2 line (200 µm), however its specific resistance was much higher than laser scribed P2 lines. The results of EDS analysis of the tweezer scribed P2 line are shown in Fig. 12. The residue of NiO_x was clearly present at the center of the P2 line. Mechanical scribing was not able to remove NiO_x, which is evidence that laser scribing process is superior to mechanical scribing method of P2 lines in PVSK solar module fabrication.

3.3 Part III. Laser Scribing of P3 Line

P3 is a scribe line to cut back electrode. The absorption of ICO back electrode is low at the wavelength of 532 nm, so instead of scribing ICO directly, the strategy was to scribe the perovskite absorber layer underneath the ICO film. The perovskite layer absorbs 532 nm light efficiently, resulting instant temperature rise and evaporation of the material, which breaks the ICO film on the top due to the thermal mechanical stress. As ICO is a brittle ceramic material and

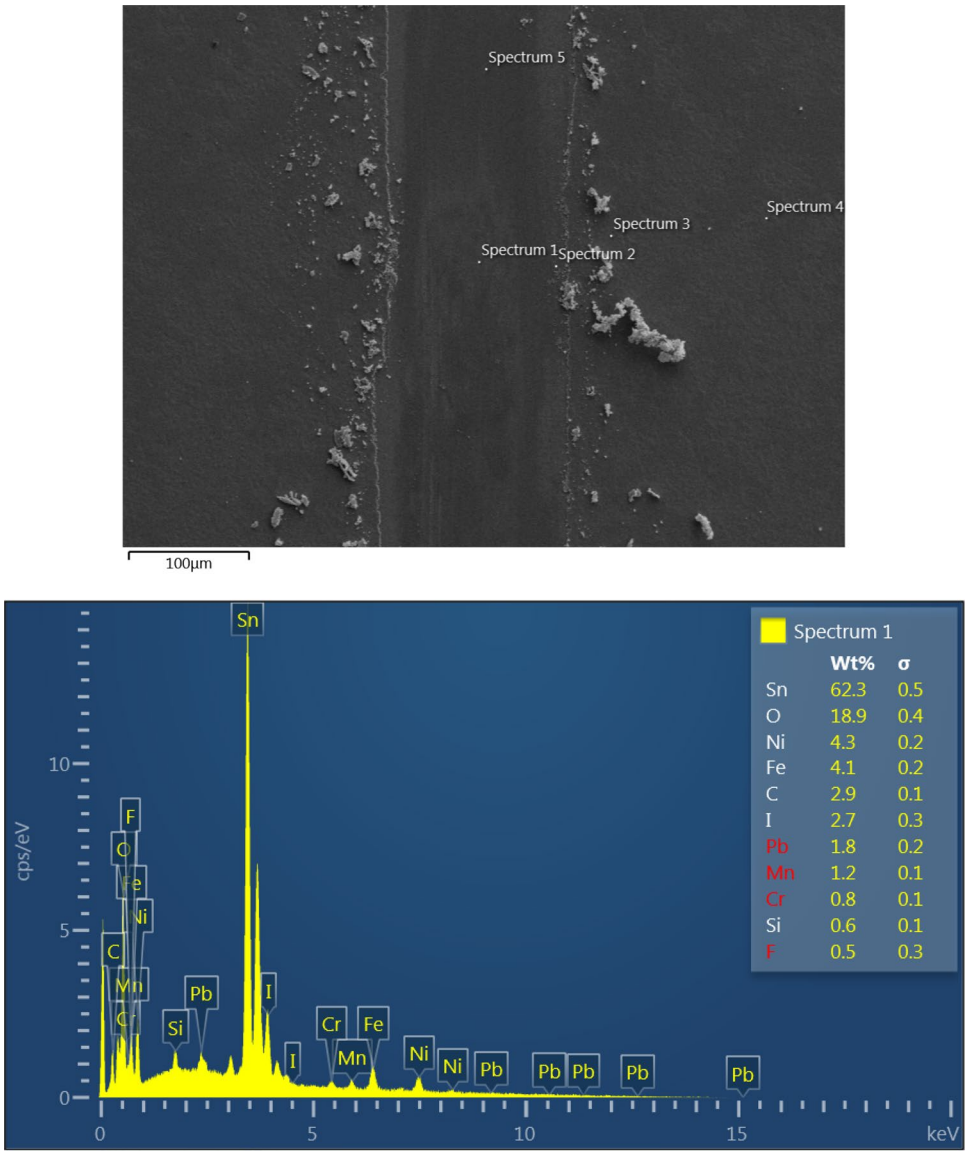

Fig. 12 SEM image and EDS elemental analysis of P2 line scribed by a tweezer

only a small portion of PVSK layer underneath ICO needs to be removed, the power density requires to break ICO is much lower than that used in P2 scribing process. The remaining perovskite film in P3 line would not affect the device performance as long as ICO is cut cleanly and well isolated.

OM images of P3 lines with various laser power densities are shown in Fig. 13. The zigzag fragmentation marks at the edges of P3 line are due to the characteristics of ceramic material. The ripple-like patterns are indication of mechanical stress in ICO film after laser scribing. P3 line width is positively correlated to the laser power density, and the chipping area also is increased with the increasing laser power as shown in Fig. 14. The lowest power density of 2.5×10^4 kW/cm^2 was selected in order to minimize the P3 line width, thus to minimize the dead area.

With a fixed laser power density at 2.5×10^4 kW/cm^2, 90, 75, 65% overlap ratio were used to scribe P3 lines. There was no much change of chipping area as shown in Fig. 15. The remains in P3 line was determined by EDS as shown in the SEM image of Fig. 16. Data in Table 5 indicates that there are remains of perovskite layer and NiO_x in P3 line, and at the center of the P3 line no Pb and I were detected, but NiO_x is still present.

3.4 Part IV. Fabrication and Evaluation of Solar Module

Bifacial perovskite modules were made on a 2×2 cm^2 substrate. The modules consisted two 5 mm cells connected in series. With fixed P1 and P3 process parameters (P1 8.78×10^5 kW/cm^2 and 91% overlap ratio, P3 2.5×10^4

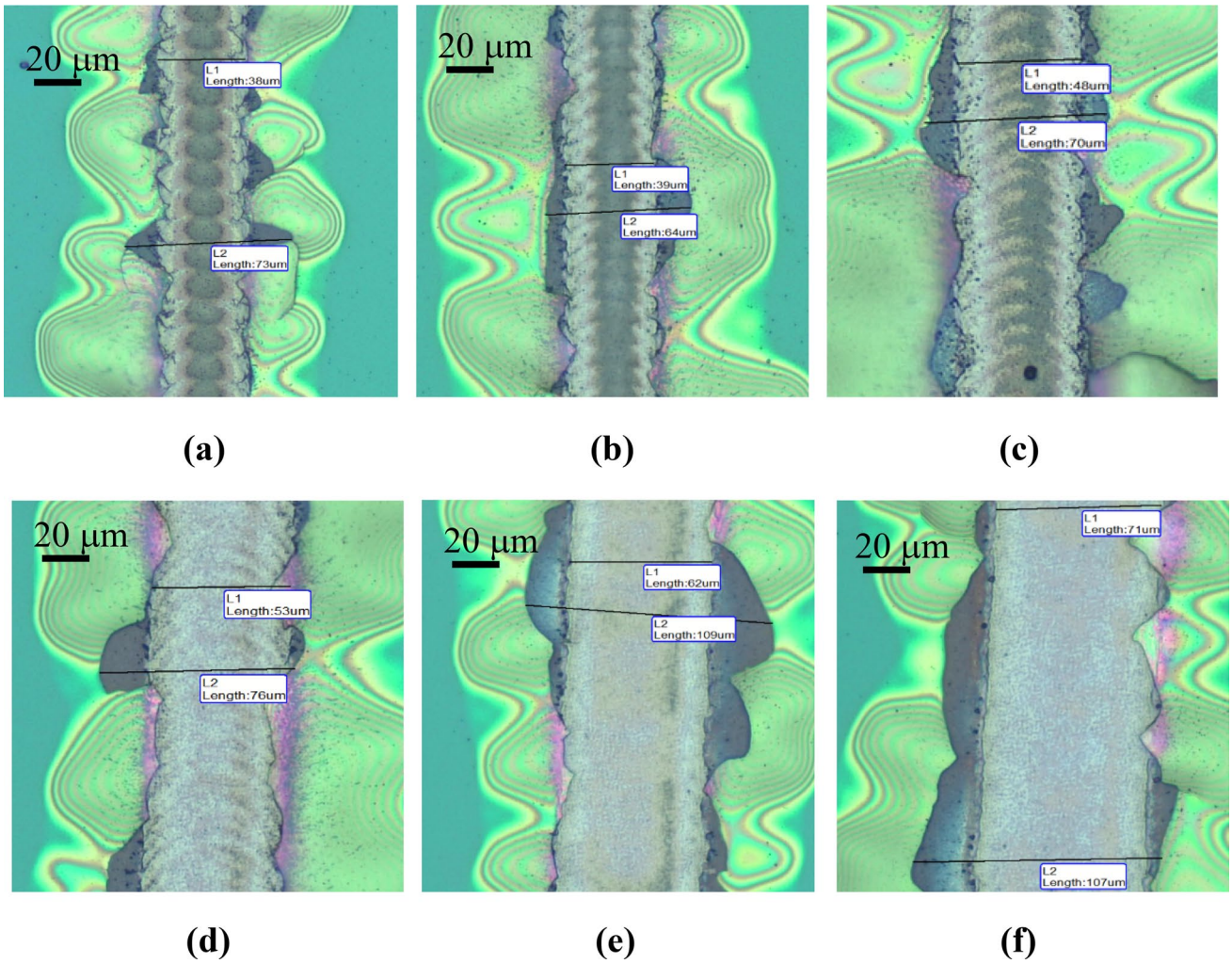

Fig. 13 OM image of P3 lines at different pulse power density **a** 2.5×10^4, **b** 4×10^4, **c** 5.99×10^4, **d** 7.7×10^4, **e** 8.99×10^4, **f** 1.15×10^5 kW/cm^2

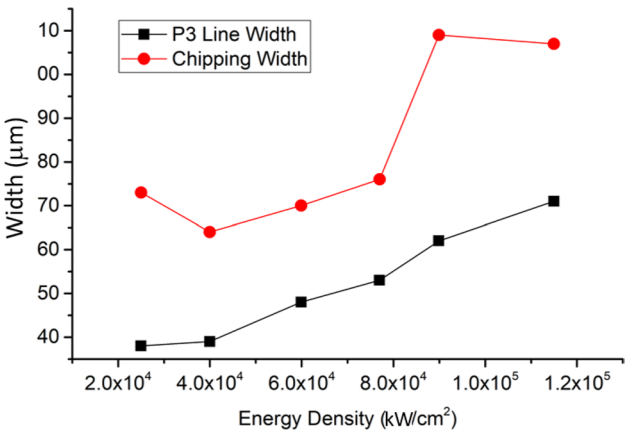

Fig. 14 Width of P3 line and chipping area as function of laser power density

kW/cm^2 and 65% overlap ratio) three different P2 process parameters were used to test the effect of contact width as shown in Table 6. The performances of the modules as well as the control group (0.09 cm^2 cell) are summarized in Table 7.

The average active area PCE of the control sample (0.09 cm^2) is 13.8% and the average FF is 70.5% as shown in Table 7. When the contact width increased from 23 μm (recipe 1) to 30 μm (recipe 2), the average FF of module increased from 60.1 to 68.2% and the average PCE increased from 9.5 to 11.6%. However, the further increase of the contact width to 41 μm (recipe 3) did not improve FF or efficiency. With contact width of 41 μm (recipe 3) the average FF is 66.0 % and the average efficiency of 11.0%. It is probably because the contact resistance at P2 interconnection was no longer the limiting factor of the total series resistance even the contact width (area) increased at P2.

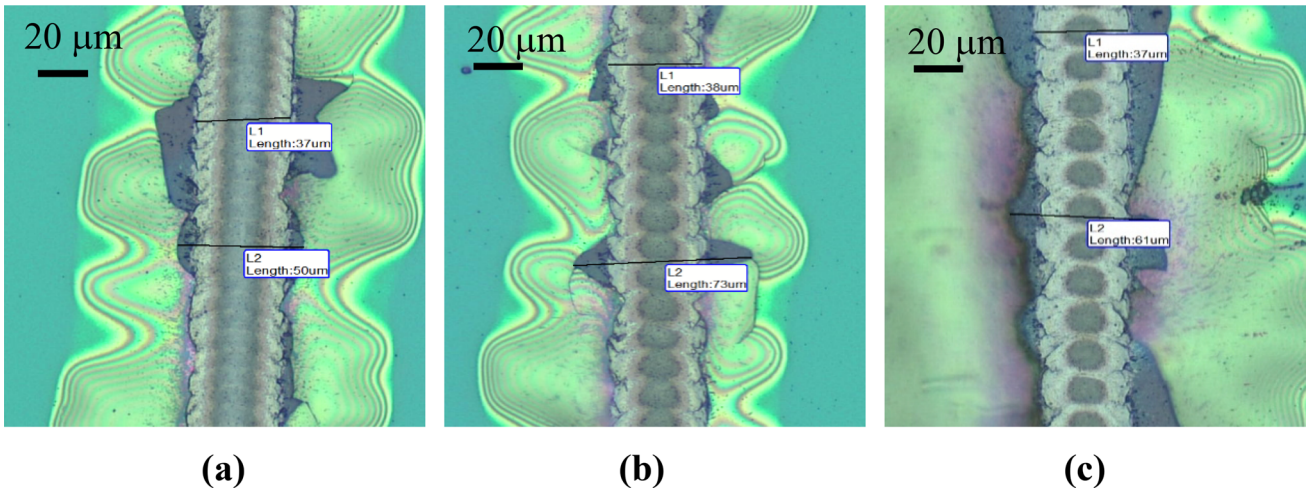

Fig. 15 OM image of P3 scribing line with **a** 90%, **b** 75%, **c** 65% overlap ratio, at a fixed laser power density of 2.5×10^4 kW/cm^2

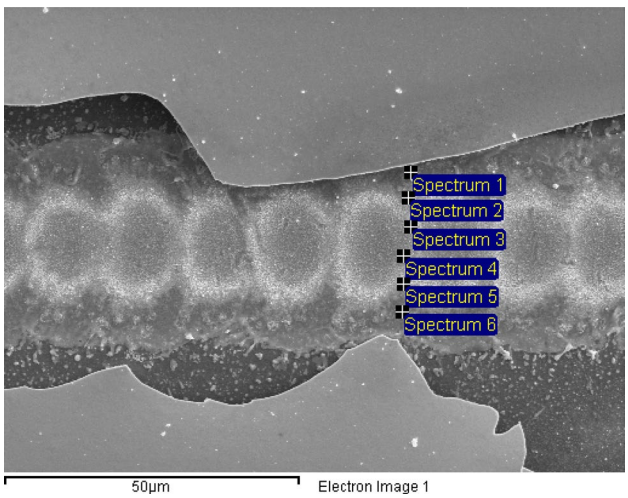

Fig. 16 SEM image of P3 line with 2.5×10^4 kW/cm^2 laser pulse power density and 65% overlap ratio

P1 and P3 had scribed the back and front electrodes with good isolation and shunting resistance are fairly high in the mini-modules. The bottom three rows show the module performance when the light was incident from ICO side of the same groups of modules, showing comparable short circuit current. External quantum efficiency (EQE) of the cells was measured and showed in Fig. 17.

J-V curves, FF and active area PCE with the above recipes are shown in Figure 18a, b and. Laser process with recipe 2 and 3 are able to achieve FF about 68% with the highest at 72.4%, similar to the small-area control sample. PCE of the two recipes are about 11%, about 2% lower than control sample mainly due to the lower J_{sc} which might be attributed to the non-uniformity of the perovskite layer formed by spin coating process. The box charts in Fig. 18c, d showed the statistical data of various samples,

Table 6 List of process parameters of P2 are used in the fabrication of module

	Laser power density (kW/cm^2)	Overlap ratio (%)	Contact width (µm)
Recipe 1	1.51×10^5	80	23
Recipe 2	2.64×10^5	73	30
Recipe 3	3.41×10^5	75	41

Table 5 Elemental analysis of different locations across P3 line

Position	Element (%)					
	O	Si	Ni	Sn	I	Pb
Spectrum 1	0.6	0.3	0.1	65.6	19.4	13.9
Spectrum 2	25.7	0.2	23.4	43.3	4.4	2.93
Spectrum 3	30.3	–	9.8	58.1	0.9	1.0
Spectrum 4	27.8	0.0	4.6	63.8	2.5	1.3
Spectrum 5	27.0	–	15.4	49.4	4.0	4.3
Spectrum 6	21.4	0.1	21.4	37.0	13.5	6.6

Table 7 Device performance of control sample and modules on 2×2 cm^2 substrate

	V_{oc} (V)[a]	J_{sc} (mA/cm^2)	FF (%)	R_s (ohm cm^2)	R_{shunt} (ohm cm^2)	PCE (%)
Control sample (active area: 0.09 cm^2)	1.04 ±0.01 (1.04)	18.2 ±0.5 (18.4)	70.5 ±3.8 (74.5)	5.9 ±0.3 (5.8)	1562 ±941 (1668)	13.8 ±0.8 (14.2)
Recipe 1 (1.1 cm^2)	1.04 ±0.01 (1.05)	15.8 ±0.8 (16.4)	60.1 ±1.6 (63.1)	72.0 ±13.1 (56.2)	4637 ±3105 (12,424)	9.5 ± 0.6 (10.8)
Recipe 2 (1.1 cm^2)	1.06 ±0.01 (1.08)	15.2 ±1.0 (16.3)	68.2 ±2.4 (71.8)	37.4 ±3.1 (34.1)	15,104 ±11, 812 (43,687)	11.6 ±0.5 (12.3)
Recipe 3 (1.1 cm^2)	1.06 ±0.01 (1.06)	16.2 ±0.7 (17.2)	66.0 ± 4.3 (69.8)	45.5 ± 11.5 (36.6)	7850 ± 3886 (11,708)	11.0 ±1.1 (12.4)
Recipe 1 (light incidents from ICO side)	1.02 ±0.02 (1.03)	16.0 ±0.5 (16.9)	62.2 ±2.9. (65.3)	59.4 ±5.5 (50.1)	20,348 ± 55,886 (180,945)	10.1 ±0.7 (11.3)
Recipe 2 (light incidents from ICO side)	1.03 ±0.02 (1.05)	16.1 ±0.1 (16.4)	70.1 ±1.9 (72.4)	37.0 ±3.7(35.0)	17,513 ± 19,384 (71,700)	12.1 ±0.3 (12.4)
Recipe 3 (light incidents from ICO side)	1.03 ±0.01 (1.04)	16.3 ±0.9 (17.4)	67.9 ±3.2 (70.8)	39.4 ± 4.3 (35.8)	26,724 ± 49,806 (166,652)	11.7 ±0.9 (12.5)

J_{sc} and PCE are measured at active area. An average value of 9 control samples and 10 module samples is present and the champion result is in bracket

[a]V_{oc} of modules is the measured open circuit voltage divided by cell numbers of 2

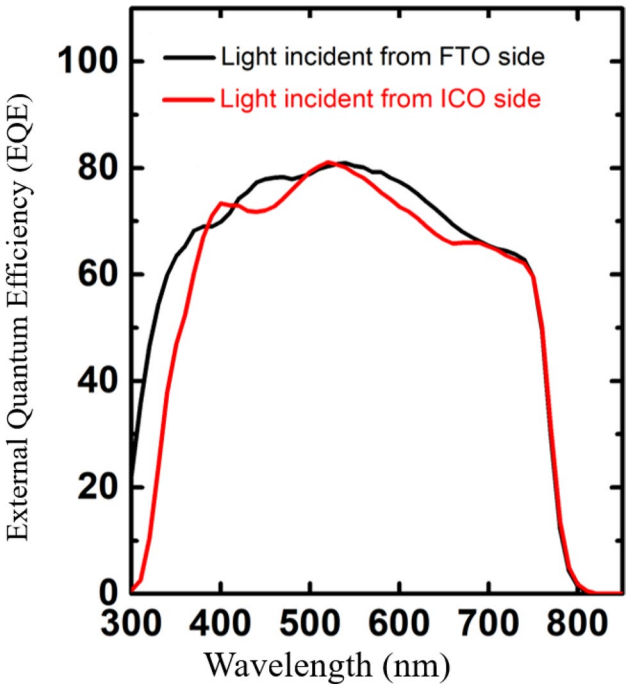

Fig. 17 External quantum efficiency (EQE) of the perovskite solar cell

implying good stability of the laser processes based on our nanosecond pulsed laser. The highest PCE of mini-modules is 12.5% and the best FF is 72.4%.

A picture of bifacial perovskite module and an OM image of three scribing lines are shown in Fig. 19. The line width of P1 was about 22 µm, the line width of P2 was 50 µm, and P3 line included about 80 µm of fragmentation width on both sides, and the overall dead zone width was 294 µm, reaching GFF of 94% with cell width of 5 mm.

4 Conclusion

We have demonstrated that a nanosecond pulsed laser with wavelength of 532 nm could successfully perform P1, P2 and P3 scribing processes in the fabrication of perovskite solar modules. Compared with picosecond laser and femtosecond laser it was more suitable for mass production because of its lower cost and more stable process window. Experimental parameters such as laser power and overlap ratio were systematically studied. The quality of scribing process on the films and devices were characterized with EDS as well as electrical measurement. The optimal P1 recipe to scribe FTO films was at a power density of 8.78×10^5 kW/cm^2 and 91% overlap ratio yielding excellent isolation. The laser power density of 1.51×10^5, 2.64×10^5, 3.41×10^5 kW/cm^2 were applied to P2 process which formed contact widths of 23, 30 and 41 µm respectively. EDS element analysis indicated successful removal

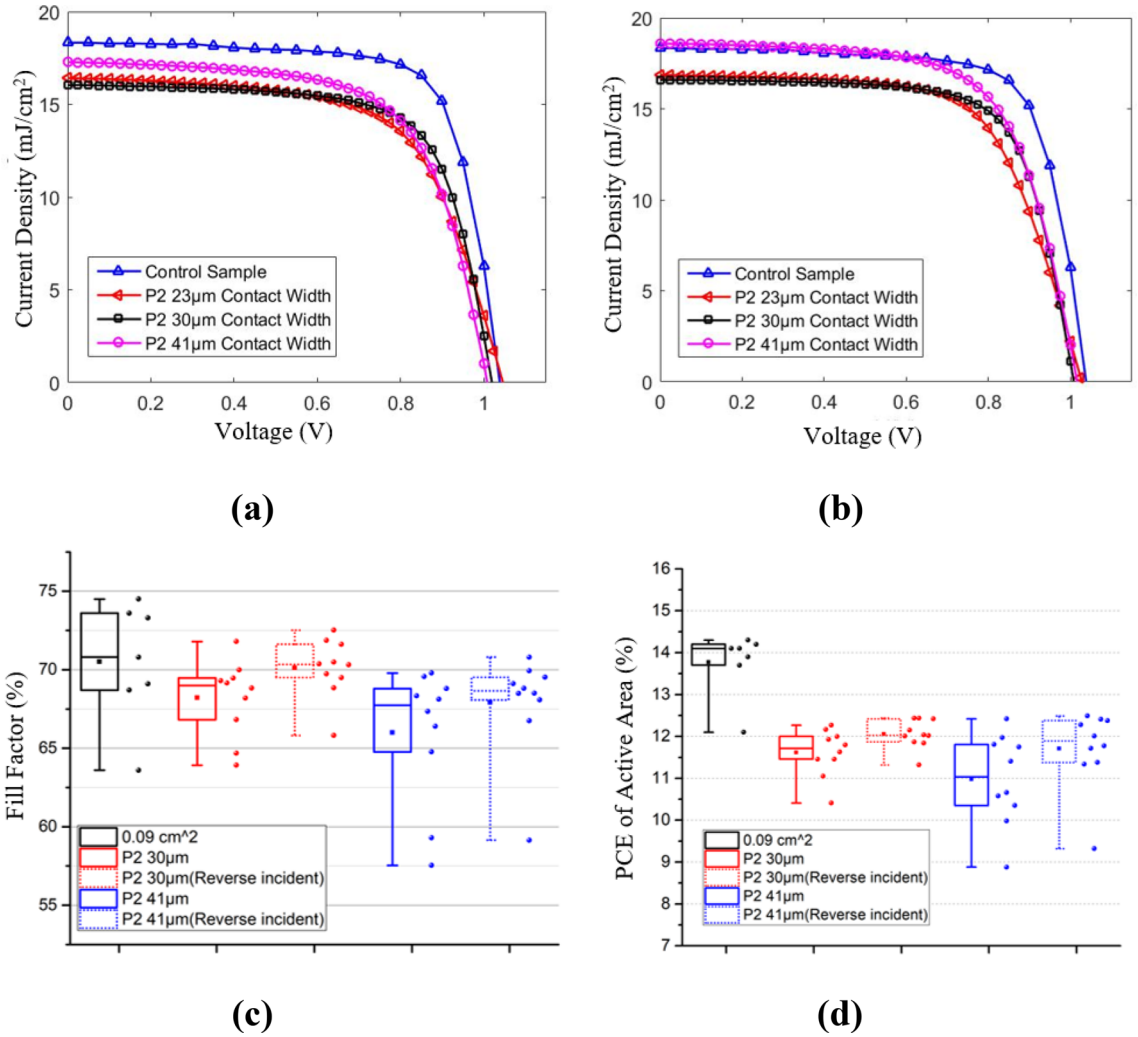

Fig. 18 **a** J–V curve of semi-transparent bifacial small area sample and modules, **b** J–V curve of ICO top electrode small area sample and modules (light incidents from ICO side). **c** Box charts of the FF, **d** box charts of the active area efficiencies

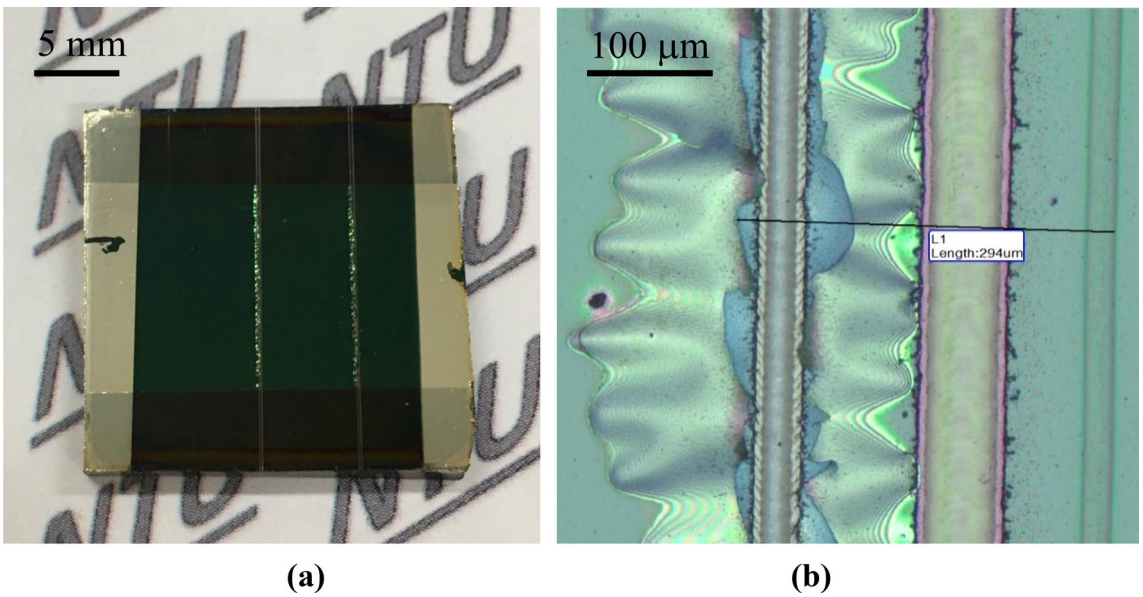

Fig. 19 **a** A picture of bifacial perovskite solar module; **b** an OM images of the three scribing lines

of the perovskite layer as well as NiO_x layer without damaging FTO films underneath. P3 was operated at 2.5×10^4 kW/cm^2 and 65% overlap ratio to isolate the transparent back electrode ICO. The dead zone width (from P1 to P3) was less than 300 µm, reaching GFF 94% with 5 mm cell width. An active area efficiency of 12.5% was achieved on the champion module and the best FF was 72.4%.

Acknowledgements This work is supported by National Taiwan University and the Ministry of Science and Technology (MOST) of Taiwan (108-3116-F-002-002-CC2).

Declarations

Conflict of interest The authors declare that they have no known competing financial interests or personal relationships that could have appeared to influence the work reported in this paper.

References

1. Kojima, A., Teshima, K., Shirai, Y., & Miyasaka, T. (2009). Organometal halide perovskites as visible-light sensitizers for photovoltaic cells. *Journal of the American Chemical Society, 131*(17), 6050–6051. https://doi.org/10.1021/ja809598r
2. Zhou, H. P., Chen, Q., Li, G., Luo, S., Song, T. B., Duan, H. S., Hong, Z. R., You, J. B., Liu, Y. S., & Yang, Y. (2014). Interface engineering of highly efficient perovskite solar cells. *Science, 345*(6196), 542–546. https://doi.org/10.1126/science.1254050
3. Jiang, Q., Chu, Z. N., Wang, P. Y., Yang, X. L., Liu, H., Wang, Y., Yin, Z. G., Wu, J. L., Zhang, X. W., & You, J. B. (2017). Planar-structure perovskite solar cells with efficiency beyond 21%. *Advanced Materials, 29*(46), 7. https://doi.org/10.1002/adma.201703852
4. Jiang, Q., Zhao, Y., Zhang, X. W., Yang, X. L., Chen, Y., Chu, Z. M., Ye, Q. F., Li, X. X., Yin, Z. G., & You, J. B. (2019). Surface passivation of perovskite film for efficient solar cells. *Nature Photonics, 13*(7), 460. https://doi.org/10.1038/s41566-019-0398-2
5. Yang, D., Zhang, X. R., Wang, K., Wu, C. C., Yang, R. X., Hou, Y. C., Jiang, Y. Y., Liu, S. Z., & Priya, S. (2019). Stable efficiency exceeding 20.6% for inverted perovskite solar cells through polymer-optimized PCBM electron-transport layers. *Nano Letters, 19*(5), 3313–3320. https://doi.org/10.1021/acs.nanolett.9b00936
6. Zhao, Y., Ye, Q. F., Chu, Z. M., Gao, F., Zhang, X. W., & You, J. B. (2019). Recent progress in high-efficiency planar-structure perovskite solar cells. *Energy and Environmental Materials, 2*(2), 93–106. https://doi.org/10.1002/eem2.12042
7. Grancini, G., Roldan-Carmona, C., Zimmermann, I., Mosconi, E., Lee, X., Martineau, D., Narbey, S., Oswald, F., De Angelis, F., Graetzel, M., & Nazeeruddin, M. K. (2017). One-year stable perovskite solar cells by 2D/3D interface engineering. *Nature Communications, 8*, 8. https://doi.org/10.1038/ncomms15684
8. Hu, H. L., Ren, Z. W., Fong, P. W. K., Qin, M. C., Liu, D. J., Lei, D. Y., Lu, X. H., & Li, G. (2019). Room-temperature meniscus coating of >20% perovskite solar cells: A film formation mechanism investigation. *Advanced Functional Materials, 29*(25), 12. https://doi.org/10.1002/adfm.201900092
9. Deng, Y. H., Peng, E., Shao, Y. C., Xiao, Z. G., Dong, Q. F., & Huang, J. S. (2015). Scalable fabrication of efficient organolead trihalide perovskite solar cells with doctor-bladed active layers. *Energy and Environmental Science, 8*(5), 1544–1550. https://doi.org/10.1039/c4ee03907f
10. Deng, Y. H., Dong, Q. F., Bi, C., Yuan, Y. B., & Huang, J. S. (2016). Air-stable, efficient mixed-cation perovskite solar cells with Cu electrode by scalable fabrication of active layer. *Advanced Energy Materials*. https://doi.org/10.1002/aenm.201600372
11. Yang, M. J., Li, Z., Reese, M. O., Reid, O. G., Kim, D. H., Siol, S., Klein, T. R., Yan, Y., Berry, J. J., van Hest, M., & Zhu, K. (2017). Perovskite ink with wide processing window for scalable high-efficiency solar cells. *Nature Energy, 2*(5), 9. https://doi.org/10.1038/nenergy.2017.38
12. Huang, S. H., Guan, C. K., Lee, P. H., Huang, H. C., Li, C. F., Huang, Y. C., & Su, W. F. (2020). Toward all slot-die fabricated high efficiency large area perovskite solar cell using rapid near infrared heating in ambient air. *Advanced Energy Materials, 10*(37), 9. https://doi.org/10.1002/aenm.202001567
13. Kim, J. E., Jung, Y. S., Heo, Y. J., Hwang, K., Qin, T. S., Kim, D. Y., & Vak, D. (2018). Slot die coated planar perovskite solar cells via blowing and heating assisted one step deposition. *Solar Energy Materials and Solar Cells, 179*, 80–86. https://doi.org/10.1016/j.solmat.2018.02.003
14. Galagan, Y., Di Giacomo, F., Gorter, H., Kirchner, G., de Vries, I., Andriessen, R., & Groen, P. (2018). Roll-to-roll slot die coated perovskite for efficient flexible solar cells. *Advanced Energy Materials, 8*(32), 7. https://doi.org/10.1002/aenm.201801935
15. Hossain, I. M., Hudry, D., Mathies, F., Abzieher, T., Moghadamzadeh, S., Rueda-Delgado, D., Schackrnar, F., Bruns, M., Andriessen, R., Aernouts, T., Di Giacomo, F., Lemmer, U., Richards, B. S., Paetzold, U. W., & Hadipour, A. (2019). Scalable processing of low-temperature TiO_2 nanoparticles for high-efficiency perovskite solar cells. *ACS Applied Energy Materials, 2*(1), 47–58. https://doi.org/10.1021/acsaem.8b01567
16. Tait, J. G., Manghooli, S., Qiu, W., Rakocevic, L., Kootstra, L., Jaysankar, M., de la Huerta, C. A. M., Paetzold, U. W., Gehlhaar, R., Cheyns, D., Heremans, P., & Poortmans, J. (2016). Rapid composition screening for perovskite photovoltaics via concurrently pumped ultrasonic spray coating. *Journal of Materials Chemistry A, 4*(10), 3792–3797. https://doi.org/10.1039/c6ta00739b
17. Cai, H. K., Liang, X. J., Ye, X. F., Su, J., Guan, J. Y., Yang, J. T., Liu, Y., Zhou, X. J., Han, R., Ni, J., Li, J., & Zhang, J. J. (2020). High efficiency over 20% of perovskite solar cells by spray coating via a simple process. *ACS Applied Energy Materials, 3*(10), 9696–9702. https://doi.org/10.1021/acsaem.0c01129
18. Zhang, Y., Kim, S. G., Lee, D., Shin, H., & Park, N. G. (2019). Bifacial stamping for high efficiency perovskite solar cells. *Energy and Environmental Science, 12*(1), 308–321. https://doi.org/10.1039/c8ee02730g
19. Li, J., Wang, H., Chin, X. Y., Dewi, H. A., Vergeer, K., Goh, T. W., Lim, J. W. M., Lew, J. H., Loh, K. P., Soci, C., Sum, T. C., Bolink, H. J., Mathews, N., Mhaisalkar, S., & Bruno, A. (2020). Highly efficient thermally co-evaporated perovskite solar cells and mini-modules. *Joule, 4*(5), 1035–1053. https://doi.org/10.1016/j.joule.2020.03.005
20. Matteocci, F., Razza, S., Di Giacomo, F., Casaluci, S., Mincuzzi, G., Brown, T. M., D'Epifanio, A., Licoccia, S., & Di Carlo, A. (2014). Solid-state solar modules based on mesoscopic organometal halide perovskite: A route towards the upscaling process. *Physical Chemistry Chemical Physics, 16*(9), 3918–3923. https://doi.org/10.1039/c3cp55313b
21. Yang, M. J., Kim, D. H., Klein, T. R., Li, Z., Reese, M. O., de Villers, B. J. T., Berry, J. J., van Hest, M., & Zhu, K. (2018). Highly efficient perovskite solar modules by scalable fabrication and interconnection optimization. *ACS Energy Letters, 3*(2), 322–328. https://doi.org/10.1021/acsenergylett.7b01221
22. Higuchi, H., & Negami, T. (2018). Largest highly efficient 203 × 203 mm(2) $CH_3NH_3PbI_3$ perovskite solar modules. *Japanese Journal of Applied Physics*. https://doi.org/10.7567/jjap.57.08re11

23. Rakocevic, L., Gehlhaar, R., Merckx, T., Qiu, W. M., Paetzold, U. W., Fledderus, H., & Poortmans, J. (2017). Interconnection optimization for highly efficient perovskite modules. *IEEE Journal of Photovoltaics, 7*(1), 404–408. https://doi.org/10.1109/jphotov.2016.2626144
24. Booth, H. (2010). Laser processing in industrial solar module manufacturing. *Journal of Laser Micro Nanoengineering, 5*(3), 183–191. https://doi.org/10.2961/jlmn.2010.03.0001
25. Turan, B., & Haas, S. (2013). Scribe width optimization of absorber laser ablation for thin-film silicon solar modules. *Journal of Laser Micro Nanoengineering, 8*(3), 234–243. https://doi.org/10.2961/jlmn.2013.03.0009
26. Turan, B., Haas, S., & Steger, M. (2014). Optimization of front-contact laser scribing for thin-film silicon solar modules. *Solar Energy Materials and Solar Cells, 125*, 78–86. https://doi.org/10.1016/j.solmat.2014.02.029
27. Kubis, P., Li, N., Stubhan, T., Machui, F., Matt, G. J., Voigt, M. M., & Brabec, C. J. (2015). Patterning of organic photovoltaic modules by ultrafast laser. *Progress in Photovoltaics, 23*(2), 238–246. https://doi.org/10.1002/pip.2421
28. Bayer, L., Ehrhardt, M., Lorenz, P., Pisoni, S., Buecheler, S., Tiwari, A. N., & Zimmer, K. (2017). Morphology and topography of perovskite solar cell films ablated and scribed with short and ultrashort laser pulses. *Applied Surface Science, 416*, 112–117. https://doi.org/10.1016/j.apsusc.2017.04.058
29. Schultz, C., Fenske, M., Dagar, J., Zeiser, A., Bartelt, A., Schlatmann, R., Unger, E., & Stegemann, B. (2020). Ablation mechanisms of nanosecond and picosecond laser scribing for metal halide perovskite module interconnection—An experimental and numerical analysis. *Solar Energy, 198*, 410–418. https://doi.org/10.1016/j.solener.2020.01.074
30. Bayer, L., Ye, X. Y., Lorenz, P., & Zimmer, K. (2017). Studies on perovskite film ablation and scribing with ns-, ps- and fs-laser pulses. *Applied Physics A-Materials Science and Processing, 123*(10), 8. https://doi.org/10.1007/s00339-017-1234-5
31. Moon, S. J., Yum, J. H., Lofgren, L., Walter, A., Sansonnens, L., Benkhaira, M., Nicolay, S., Bailat, J., & Ballif, C. (2015). Laser-scribing patterning for the production of organometallic halide perovskite solar modules. *IEEE Journal of Photovoltaics, 5*(4), 1087–1092. https://doi.org/10.1109/jphotov.2015.2416913
32. Palma, A. L., Matteocci, F., Agresti, A., Pescetelli, S., Calabro, E., Vesce, L., Christiansen, S., Schmidt, M., & Di Carlo, A. (2017). Laser-patterning engineering for perovskite solar modules with 95% aperture ratio. *IEEE Journal of Photovoltaics, 7*(6), 1674–1680. https://doi.org/10.1109/jphotov.2017.2732223
33. Palma, A. L. (2020). Laser-processed perovskite solar cells and modules. *Solar RRL, 4*(4), 19. https://doi.org/10.1002/solr.201900432
34. Liu, X., Du, D., & Mourou, G. (1997). Laser ablation and micromachining with ultrashort laser pulses. *IEEE Journal of Quantum Electronics, 33*(10), 1706–1716. https://doi.org/10.1109/3.631270
35. Wang, C., Tan, G. Y., Luo, X. P., Li, J., Gao, X. F., Mo, Y. P., Zhang, X. L., Wang, X. W., & Huang, F. Z. (2020). How to fabricate efficient perovskite solar mini-modules in lab. *Journal of Power Sources, 466*, 7. https://doi.org/10.1016/j.jpowsour.2020.228321
36. Spyropoulos, G. D., Quiroz, C. O. R., Salvador, M., Hou, Y., Gasparini, N., Schweizer, P., Adams, J., Kubis, P., Li, N., Spiecker, E., Ameri, T., Egelhaaf, H. J., & Brabec, C. J. (2016). Organic and perovskite solar modules innovated by adhesive top electrode and depth-resolved laser patterning. *Energy and Environmental Science, 9*(7), 2302–2313. https://doi.org/10.1039/c6ee01555g
37. Lee, P. H., Wu, T. T., Tian, K. Y., Li, C. F., Hou, C. H., Shyue, J. J., Lu, C. F., Huang, Y. C., & Su, W. F. (2020). Work-function-tunable electron transport layer of molecule-capped metal oxide for a high-efficiency and stable p-i-n perovskite solar cell. *ACS Applied Materials and Interfaces, 12*(41), 45936–45949. https://doi.org/10.1021/acsami.0c10717
38. Jeng, J. Y., Chen, K. C., Chiang, T. Y., Lin, P. Y., Tsai, T. D., Chang, Y. C., Guo, T. F., Chen, P., Wen, T. C., & Hsu, Y. J. (2014). Nickel oxide electrode interlayer in $CH_3NH_3PbI_3$ perovskite/pcbm planar-heterojunction hybrid solar cells. *Advanced Materials, 26*(24), 4107–4113. https://doi.org/10.1002/adma.201306217
39. Ben-Yakar, A., & Byer, R. L. (2004). Femtosecond laser ablation properties of borosilicate glass. *Journal of Applied Physics, 96*(9), 5316–5323. https://doi.org/10.1063/1.1787145

Bo-Qian Lin who graduated from National Taiwan University with Master's degree in 2021 and had two years of solar cell fabrication experience, currently is working at Via Next Technologies, Inc. (New Taipei City, Taiwan).

Chao-Peng Huang received his M.S. in Mechanical Engineering from National Taiwan University in 2021. Currently he is an engineer in New Energy Research Department of Zhejiang Energy R&D Institute Co. Ltd. (Hanzhou, Zhejiang Province, China). His main research interests include laser patterning technologies, perovskite solar cells and photovoltaic systems.

Kuo-Yo Tian who graduated from National Taiwan University with Master's degree in 2016, had been as research assistant in Prof. Su's lab until 2019. He had four years of perovskite solar cell sub-module fabrication experience.

Pei-Huan Lee received his Ph.D. in Materials Science and Engineering from National Taiwan University, Taipei, Taiwan, in 2021. His research interests focus on synthesis of nano-material, thin film technology and perovskite solar cell.

Wei-Fang Su received her Ph.D. from University of Massachusetts, Amherst, MA, USA in 1978 and did postdoctoral research in Northwestern University, Evanston, IL, USA in 1979. She worked in Westinghouse R&D Center, Pittsburgh, PA, USA for 16 years. She joined the National Taiwan University as a full professor in 1996 and retired as a distinguished professor in 2021. Currently, she is a Visiting Chair Professor of Ming-Ching University of Technology, Taiwan. Her specialty is material development for electronic devices, solar cells and biomedicines. She has contributed 240 scientific publications, two textbooks and over 80 patents.

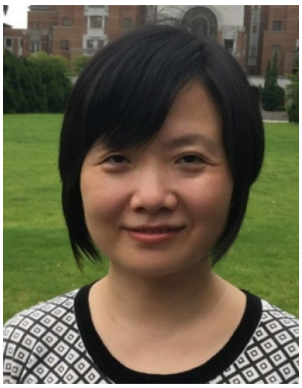

Li Xu received her Ph.D. from University of California, Berkeley, CA USA in 2006. She has been working in Applied Materials Inc. (Santa Clara, CA, USA) for 5 years and TSMC Solar Inc. (Taichung City, Taiwan) for about 6 years. She joined the National Taiwan University as an assistant professor in 2018. Her specialty is laser material processing, photovoltaic systems, flexible devices. She has contributed 7 scientific publications and 5 U.S. patents.